Electronic Supplementary Material (ESI) for Environmental Science: Nano.

Electronic Supplementary Information (ESI)

Visualization of Transport and Fate of Nano and Micro Scale Particles in Porous Media: Modeling Coupled Effects of Ionic Strength and Size with Force Analysis

Chen Chen[a] , *Travis Waller*[a], *and Sharon L. Walker*[a]*

[a]Department of Chemical and Environmental Engineering, University of California, Riverside, Riverside, CA,
92521

*Corresponding author: Sharon L. Walker, University of California, Riverside, Riverside, CA
Email: swalker@engr.ucr.edu

Number of Pages: 15; Number of Figures: 3 Number of Table: 2

Materials and Methods

DLVO Calculations DLVO theory was applied to calculate the total interaction energy (sum of London-van der Waals attraction and electrostatic double-layer forces)[1] for particles upon close approach to the collector surface as a function of separation distance[1,2].

$$\Phi_{total}(h) = \Phi_{el}(h) + \Phi_{vdW}(h) \qquad [1]$$

where Φ_{total} [M L^2 T^{-2}], Φ_{el} [M L^2 T^{-2}], and Φ_{vdW} [M L^2 T^{-2}] are the total, electrostatic, and van der Waals interaction energies, respectively, and h [L] is the separation distance between the latex microspheres and the surface of quartz collectors. Values of Φ_{total}, Φ_{el}, and Φ_{vdW} are commonly made dimensionless by dividing by the product of the Boltzmann constant ($k_B = 1.38 \times 10^{-23}$ J K^{-1}) and the absolute temperature (T_K).

For a sphere-plate interaction, the electrostatic double layer interactions can be determined with the constant surface potential interaction expression of Hogg[3] as

$$\Phi_{el}(h) = \frac{\pi r_1 r_2}{(r_1 + r_2)} \left\{ 2\phi_1\phi_2 \ln\left[\frac{1+\exp(-\kappa h)}{1-\exp(-\kappa h)}\right] + \left(\phi_1^2 + \phi_2^2\right) \ln\left[1 - \exp\left(-2\kappa h\right)\right] \right\} \qquad [2]$$

where r_1 [L] is the radius of a latex microsphere, r_2 [L] is the radius of the collector, ϕ_1 [M L^2 T^{-3} A^{-1}] is the surface potential of the latex microsphere, ϕ_2 [M L^2 T^{-3} A^{-1}] is the surface potential of the collector, and κ [L^{-1}] is the Debye–Huckel parameter. Measured zeta potentials were used in place of surface potentials in Eq. [1].

The van der Waals interaction energy Φ_{vdW} was determined using the expression by Gregory[2] as

$$\Phi_{vdW}(h) = \frac{A_{123} r_1}{6h} \left\{ 1 + \frac{14h}{\lambda} \right\}^{-1} \qquad [3]$$

where A_{123} [M L^2 T^{-2}] is the Hamaker constant in this system, and λ [L] is the characteristic wavelength that is often taken as 100 nm (Gregory, 1981). A value of 4.04×10^{-21} J for the Hamaker constant of the latex-quartz-water system was determined by using

$$A_{123} = (\sqrt{A_{11}} - \sqrt{A_{33}})(\sqrt{A_{22}} - \sqrt{A_{33}}) \qquad [4]$$

where A_{11}, A_{22}, and A_{33} is the Hamaker constant of latex, quartz and water in vacuum, respectively. The value of these Hamaker constants was gained from the results of the theoretical calculation approximation for Hamaker constants[4,5].

Correlation Equation for Predicting Single Collector Efficiency

The transport and deposition of particles in saturated porous media is described by the convective-diffusion equation. Under steady-state condition, the dimensionless convection-diffusion equation can be expressed as[6,7]:

$$\eta_0 = \eta_0(N_R, N_{Pe}, N_{vdW}, N_{gr}) \qquad [5]$$

The definitions of these parameters are provided in Table S1. Based on the additivity assumption previously presented[6,8], the overall single collector removal efficiency can be decided by summing each transport mechanism (including diffusion, interception and gravitational transport mechanisms). The methodology for each transport mechanisms correlation equations is shown as follows:

For diffusion, the correlation has been determined as:

$$\eta_D = 2.4 A_S^{1/3} N_R^{-0.081} N_{Pe}^{-0.715} N_{vdW}^{-0.052} \qquad [6]$$

It is interesting to find that based on the eq S6, $\eta_D \sim d_p^{-0.796}$ (compared to $\eta_D \sim d_p^{-0.666}$ of classic method[9]), which indicates the significant influence of hydrodynamic interactions on particle deposition.

Similarly, for interception, the expression was shown as:

$$\eta_I = 0.55 A_S N_R^{1.55} N_{Pe}^{-0.125} N_{vdW}^{-0.125} \qquad [7]$$

For gravitational transport mechanism,

$$\eta_G = 0.475 N_R^{-1.35} N_{Pe}^{-1.11} N_{vdW}^{0.053} N_{gr}^{1.11} \qquad [8]$$

The overall single collector removal efficiency for deposition in saturated porous media can now be written as the sum of each transport mechanism (eqs S6-S8):

$$\eta_0 = 2.4 A_S^{1/3} N_R^{-0.081} N_{Pe}^{-0.715} N_{vdW}^{-0.052} + 0.55 A_S N_R^{1.55} N_{Pe}^{-0.125} N_{vdW}^{-0.125} + 0.475 N_R^{-1.35} N_{Pe}^{-1.11} N_{vdW}^{0.053} N_{gr}^{1.11} \quad [9]$$

Velocity Distribution Calculation with COMSOL

COMSOL was used to simulate the velocity distribution around the collector. The assumption was made that the bulk solution in the 2D micromodel system is stationary with no pressure drop in the system. Therefore, the relevant expressions are as follows[11]:

$$\rho(\mathrm{u}\cdot\nabla)\mathrm{u}=\nabla\cdot[-pI+\mu(\nabla\mathrm{u}+(\nabla\mathrm{u})^T-\frac{2}{3}\mu(\nabla\cdot\mathrm{u})I] \quad [10]$$

$$I=\frac{1}{2}(1-c^2) \quad [11]$$

$$c=\frac{\delta+\mu}{\delta+1} \quad [12]$$

$$\nabla\cdot(\rho\mathrm{u})=0 \quad [13]$$

Where a stream of fluid with velocity u, density ρ, viscosity μ and absolute temperature T over the micromodel system. Boundary-layer thickness is represented by δ , and I and c are symbols defined in Eq. 6 and 7[11].

Boundary conditions:

u=0 at the position x=1, when solution first entered the 2D micromodel system,

u= =-U$_{max}$ [1-(2y/h)^2], the bulk solution velocity at the position of X=35 µm (or half the width of the pore throat), h is the separation distance between particle and collector.

Specifically, the velocity of each point around the collector surface was determined through simulations using COMSOL (results of the simulation are presented in Figure S2b). These values of velocity were then used for the calculation of the lift and drag forces (Eq. 2-3) at every point from the collector surface to the bulk fluid in the 2-D system. Additionally, the lift and drag forces at a few representative points around the collector surface have been calculated and are presented in the manuscript (Figure 5). With these calculated fluid forces, a force balance was done on individual nanoparticles as they travel along the collector grain and within the pore throat.

Results and Discussion

Velocity and Acceleration Distribution

In order to calculate the hydrodynamic forces (lift force and drag force), the velocity distributions and acceleration as a function of x position as well as distance from surface are pictured in Figure S2. COMSOL has been used to simulate the velocity distribution (shown in Figure S2a) where the red arrow indicates the flow direction.

According to Figure S2a, the corresponding velocity distribution as a function of distance around the collector surface has been plotted in Figure S2b. The velocity of each point around the collector surface was determined through simulations using COMSOL (results of simulation are presented in Figure S2b). These values of velocity were then used to calculate the lift and drag forces (Eq. 2-3) at every point from the collector surface to bulk fluid in the 2-D system. Additionally, lift and drag forces at a few representative points around collector surface have been calculated and are presented in the manuscript (Figure 5). With these calculated fluid forces, a further force balance was done for individual moving nanoparticles as they travel along the collector grain and within the pore throat.

Calculations were done either for the entire collector surface or for a portion of the surface identified as quadrants 1-4. The portion of surface contained in quadrant 1 represents an X position ranging from 355 to 330 µm. Quadrants 2 and 4 are represented by X values from 330 to 265 µm and similarly, quadrant 3 is represented by X values from 265 to 250 µm. For a given X position, the velocity increases with the distance from the collector due to lower shear forces compared to the non-slip conditions at the surface.

Figure S3b shows that at distances from the collector surface between 0.5-10 nm, velocity decreases as expected as the fluid flows along quadrant 1 before becoming relatively constant at quadrants 2 and 4. Upon reaching quadrant 3, a slight increase in velocity was observed. Alternatively, at a 50 nm distance from collector surface, the flowrate represents the bulk flow in the micromodel. Generally, velocity increases with greater particle distance from the collector surface; however, for the closest surface distances of 0 and 0.1 nm, the velocity at an x position of 280 µm is greater than the distances farther from the collector. This observation potentially results from a decrease in the pore throat depth between collector grains causing an acceleration of the fluid flow according to Bernoulli equation[10]

Based on the velocity distribution (Figure S2b), acceleration as a function of distance from the collector surface has been plotted against x position (Figure S2c). Quadrant 3 recorded the greatest acceleration while quadrants 2 and 4 are relatively low. The velocity and acceleration data has been used to calculate the hydrodynamic forces by equations 2 and 3, respectively.

Contribution of DLVO-type Interaction and Hydrodynamic Forces

Figure S3 (b) and (d) show that at the same ionic strength, F_Y approaches zero as the angle increases between 0~120° representing quadrant 1 entirely (0-45°) and a portion of quadrant 2 (45-135°). It can be observed that positive F_Y forces (repulsive, see Figure 2) dominate at angles up to 120° before negative F_Y (attractive) forces take control. After 120^o, the magnitude of the negative forces increases with the angle accounting for the remainder of quadrant 2 (120-135^o) and quadrant 3, each controlled by attractive forces.

Moreover, the force on the x axis (F_x; eq5) in Figure S3 (a) and (c) remains negative (drag) between 0-100° indicating that for all of quadrant 1(0-45°) and part of the quadrants 2 and 4 (45-100°), the particles are inclined to roll backwards from quadrants 2 and 4 to quadrant 1. For 100-120°, which represents quadrants 2 and 4, F_x became positive and increased with the angle. This indicates that the particles tend to move from quadrant 2 and 4 towards to quadrant 3 in the flow direction. Within the range of 100 to 180^o, F_x remained positive, however decreased as the angle became greater demonstrating that particles were still prone to move with the fluid streamlines (from 2 to 3), yet with a declining magnitude. The agreement between experimental and theoretical results is acceptable for the entire range of ionic strengths with the collector surface (all four quadrants). Compliance of the experimental and theoretical results shown in Figure S3b seems to confirm the applicability of the hydrodynamic and DLVO force solutions for particle deposition in the micromodel. It should be mentioned that the significant change (positive or negative) in forces of x and y axis with fluid streamlines, is particularly due to the flow distribution around the collector surface. The influence of particle size on deposition has also been systematically studied. Comparison plots of total forces in x and y directions as a function of particles size (20, 200, 2000 nm) was pictured against with angle (0 to 180^{o}) at an ionic strength of 10 mM (Figure S3c and d, respectively). Magnitude of both F_x and F_y increase with size which illustrates that more deposition around the collector would occur with larger particles. Specifically, shown in Figure S3d, the F_y increases significantly with size after 120° and remains negative meaning 2000 nm particles are more likely to attach in quadrant 3 than the smaller particles. This suggests that the experimental results obtained in the micromodel can be used as useful reference measurements for prediction of particle deposition onto the collector surface. This work can also shows that hydrodynamic and DLVO force analysis can be exploited as powerful methods for determining filtration parameters in porous media.

Table S1. Summary of dimensionless parameters governing particles in filtration

Table S2. Summary of hydrodynamic forces and F_x, F_y as a function of size and ionic strength

Figure S1. Hydrodynamic diameter of latex particles (20, 200, 2000 nm) at ionic strengths of 1, 3.16, 10, 31.6, and100 mM KCl at pH 4.

Figure S2. Velocity distribution simulated in COMSOL as a function of (a) x position, and a function of (b) distance from surface. Acceleration was plotted as a function as x position as well as distance from collector surface (c). The portion of surface for quadrant 1 is represented a range of x position from 355 to 330 µm. Surface portions of quadrants 2 and 4 are represented by x values from 330 to 265 µm. Surface portions of quadrant 3 are represented by x value from 265 to 250 µm.

Figure S3. Total forces on 200 and 2000 nm particles in the x and y directions as a function of ionic strength (1, 3.16, 10, 31.6, and100 mM KCl) at collector surface angles between 0-180°. Forces on 200 nm particles in (a) F_x and (b) F_y, as well as, 2000 nm particles; (c) F_x and (d) F_y are presented. ,

Table S1.

Parameter	Definition	Physical interpretation
N_R	$\frac{d_p}{d_c}$	Aspect ratio
N_{Pe}	$\frac{Ud_c}{D_\infty}$	Peclet number: ratio of convection transport to diffusive transport
N_{vdW}	$\frac{A}{kT}$	van der Waals number: ratio of van der Waals interaction energy to the particle's thermal energy
N_{gr}	$\frac{4}{3}\frac{\pi a_p^4(\rho_p-\rho_f)g}{kT}$	Gravitational number: ratio of particle's gravitational potential when located one particle radius from collector to particle's thermal energy
N_A	$\frac{A}{12\pi\mu a_p^2 U}$	Attraction number: combined influence of van der Waals attraction forces and fluid velocity on particles deposition rate due to interception
N_G	$\frac{2}{9}\frac{a_p^2(\rho_p-\rho_f)g}{\mu U}$	Gravity number: ratio of Stokes particle settling velocity to approach velocity of the fluid

The parameters in various dimensionless groups are as follows: d_p is the particle diameter, d_c is the collector diameter, U is the fluid approach velocity, D_∞ is the bulk diffusion coefficient (Stokes-Einstein equation), A is the Hamaker constant, k is the Boltzmann constant, T is fluid absolute temperature, a_p is particle radius, ρ_p is the particle density, ρ_f is the fluid density, μ is the absolute fluid viscosity, and

g is the gravitational acceleration.

Table S2.

				1 mM			3.16 mM			10 mM			31.6 mM			100 mM		
Size (nm)	Angle (^{0})	F_L (N)	F_{D20nm}(N)	F_{DLVO} (N)	F_x (N)	F_y (N)	F_{DLVO} (N)	F_x (N)	F_y (N)	F_{DLVO} (N)	F_x (N)	F_y (N)	F_{DLVO} (N)	F_x (N)	F_y (N)	F_{DLVO} (N)	F_x (N)	F_y (N)
	30	1.11E-30	2.19E-23	-4.80E-11	2.38E-11	-4.10E-11	-8.40E-11	4.21E-11	-7.30E-11	-9.30E-11	4.67E-11	-8.10E-11	-1.00E-10	5.21E-11	-9.00E-11	-1.50E-10	7.39E-11	-1.30E-10
	45	1.23E-29	1.20E-22	-4.80E-11	3.37E-11	-3.40E-11	-8.40E-11	5.95E-11	-5.90E-11	-9.30E-11	6.60E-11	-6.60E-11	-1.00E-10	7.37E-11	-7.40E-11	-1.50E-10	1.04E-10	-1.00E-10
	60	1.89E-33	2.95E-25	-4.80E-11	4.12E-11	-2.40E-11	-8.40E-11	7.29E-11	-4.20E-11	-9.30E-11	8.09E-11	-4.70E-11	-1.00E-10	9.03E-11	-5.20E-11	-1.50E-10	1.28E-10	-7.40E-11
20	90	9.83E-35	-3.20E-26	-4.80E-11	4.76E-11	-2.90E-27	-8.40E-11	8.41E-11	-5.20E-27	-9.30E-11	9.34E-11	-5.70E-27	-1.00E-10	1.04E-10	-6.40E-27	-1.50E-10	1.48E-10	-9.10E-27
	120	2.72E-31	9.53E-24	-4.80E-11	-4.10E-11	2.38E-11	-8.40E-11	-7.30E-11	4.21E-11	-9.30E-11	-8.10E-11	4.67E-11	-1.00E-10	-9.00E-11	5.21E-11	-1.50E-10	-1.30E-10	7.39E-11
	135	9.83E-35	-3.20E-26	-4.80E-11	-3.40E-11	3.37E-11	-8.40E-11	-5.90E-11	5.95E-11	-9.30E-11	-6.60E-11	6.60E-11	-1.00E-10	-7.40E-11	7.37E-11	-1.50E-10	-1.00E-10	1.04E-10
	150	1.52E-30	9.98E-24	-4.80E-11	-2.40E-11	4.12E-11	-8.40E-11	-4.20E-11	7.29E-11	-9.30E-11	-4.70E-11	8.09E-11	-1.00E-10	-5.20E-11	9.03E-11	-1.50E-10	-7.40E-11	1.28E-10
	180	2.19E-31	-2.00E-23	-4.80E-11	1.97E-23	4.76E-11	-8.40E-11	1.97E-23	8.41E-11	-9.30E-11	1.97E-23	9.34E-11	-1.00E-10	1.97E-23	1.04E-10	-1.50E-10	1.97E-23	1.48E-10
	30	1.11E-27	2.19E-21	2.55E-10	-1.30E-10	2.21E-10	-5.80E-10	2.88E-10	-5.00E-10	-6.30E-10	3.13E-10	-5.40E-10	-1.30E-09	6.59E-10	-1.10E-09	-1.50E-09	7.39E-10	-1.30E-09
	45	1.23E-26	1.20E-20	2.55E-10	-1.80E-10	1.81E-10	-5.80E-10	4.08E-10	-4.10E-10	-6.30E-10	4.43E-10	-4.40E-10	-1.30E-09	9.32E-10	-9.30E-10	-1.50E-09	1.04E-09	-1.00E-09
	60	1.89E-30	2.95E-23	2.55E-10	-2.20E-10	1.28E-10	-5.80E-10	4.99E-10	-2.90E-10	-6.30E-10	5.42E-10	-3.10E-10	-1.30E-09	1.14E-09	-6.60E-10	-1.50E-09	1.28E-09	-7.40E-10
200	90	9.83E-32	-3.20E-24	2.55E-10	-2.60E-10	1.56E-26	-5.80E-10	5.76E-10	-3.50E-26	-6.30E-10	6.26E-10	-3.80E-26	-1.30E-09	1.32E-09	-8.10E-26	-1.50E-09	1.48E-09	-9.10E-26
	120	2.72E-28	9.53E-22	2.55E-10	2.21E-10	-1.30E-10	-5.80E-10	-5.00E-10	2.88E-10	-6.30E-10	-5.40E-10	3.13E-10	-1.30E-09	-1.10E-09	6.59E-10	-1.50E-09	-1.30E-09	7.39E-10
	135	9.83E-32	-3.20E-24	2.55E-10	1.81E-10	-1.80E-10	-5.80E-10	-4.10E-10	4.08E-10	-6.30E-10	-4.40E-10	4.43E-10	-1.30E-09	-9.30E-10	9.32E-10	-1.50E-09	-1.00E-09	1.04E-09
	150	1.52E-27	9.98E-22	2.55E-10	1.28E-10	-2.20E-10	-5.80E-10	-2.90E-10	4.99E-10	-6.30E-10	-3.10E-10	5.42E-10	-1.30E-09	-6.60E-10	1.14E-09	-1.50E-09	-7.40E-10	1.28E-09
	180	2.19E-28	-2.00E-21	2.55E-10	1.97E-21	-2.60E-10	-5.80E-10	1.97E-21	5.76E-10	-6.30E-10	1.97E-21	6.26E-10	-1.30E-09	1.97E-21	1.32E-09	-1.50E-09	1.97E-21	1.48E-09
	30	1.11E-24	2.19E-19	-2.40E-09	1.22E-09	-2.10E-09	-9.10E-09	4.53E-09	-7.80E-09	-1.40E-08	7.16E-09	-1.20E-08	-1.00E-08	5.00E-09	-8.70E-09	-1.50E-08	7.40E-09	
	45	1.23E-23	1.20E-18	-2.40E-09	1.73E-09	-1.70E-09	-9.10E-09	6.40E-09	-6.40E-09	-1.40E-08	1.01E-08	-1.00E-08	-1.00E-08	7.07E-09	-7.10E-09	-1.50E-08	1.05E-08	-1.00E-08
	60	1.89E-27	2.95E-21	-2.40E-09	2.12E-09	-1.20E-09	-9.10E-09	7.84E-09	-4.50E-09	-1.40E-08	1.24E-08	-7.20E-09	-1.00E-08	8.66E-09	-5.00E-09	-1.50E-08	1.28E-08	-7.40E-09
2000	90	9.83E-29	-3.20E-22	-2.40E-09	2.45E-09	-1.50E-25	-9.10E-09	9.05E-09	-5.50E-25	-1.40E-08	1.43E-08	-8.80E-25	-1.00E-08	1.00E-08	-6.10E-25	-1.50E-08	1.48E-08	-9.10E-25
	120	2.72E-25	9.53E-20	-2.4E-09	-2.1E-09	1.22E-09	-9.1E-09	-7.8E-09	4.53E-09	-1.40E-08	-1.20E-08	7.16E-09	-1.00E-08	-8.70E-09	5.00E-09	-1.50E-08	-1.30E-08	7.40E-09
	135	9.83E-29	-3.2E-22	-2.4E-09	-1.7E-09	1.73E-09	-9.1E-09	-6.4E-09	6.40E-09	-1.40E-08	-1.00E-08	1.01E-08	-1.00E-08	-7.10E-09	7.07E-09	-1.50E-08	-1.00E-08	1.05E-08
	150	1.52E-24	9.98E-20	-2.4E-09	-1.2E-09	2.12E-09	-9.1E-09	-4.5E-09	7.84E-09	-1.40E-08	-7.20E-09	1.24E-08	-1.00E-08	-5.00E-09	8.66E-09	-1.50E-08	-7.40E-09	1.28E-08
	180	2.19E-25	-2E-19	-2.4E-09	1.97E-19	2.45E-09	-9.1E-09	1.97E-19	9.05E-09	-1.40E-08	1.97E-19	1.43E-08	-1.00E-08	1.97E-19	1.00E-08	-1.50E-08	1.97E-19	1.48E-08

189 **Figure S1.**

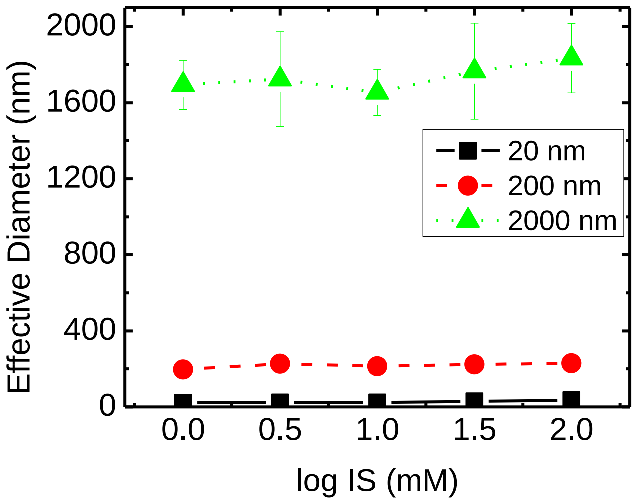

Figure S2.

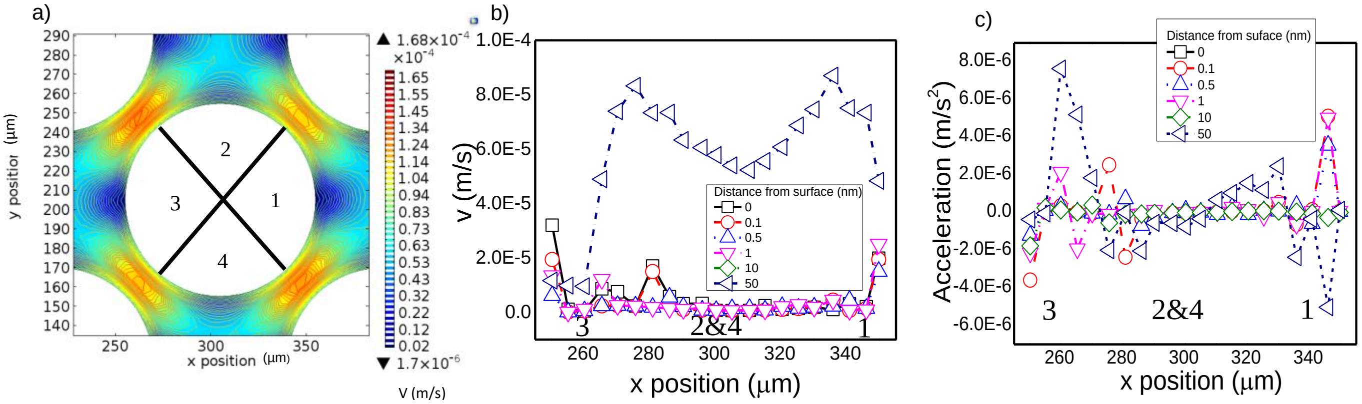
a)
290
280
270
260
250
240
230
220
210
200
190
180
170
160
150
140
y position (μm)
250
300
350
x position (μm)
2
3
1
4
1.68×10⁻⁴
×10⁻⁴
1.65
1.55
1.45
1.34
1.24
1.14
1.04
0.94
0.83
0.73
0.63
0.53
0.43
0.32
0.22
0.12
0.02
1.7×10⁻⁶
V (m/s)
b)
1.0E-4
8.0E-5
6.0E-5
4.0E-5
2.0E-5
0.0
v (m/s)
260
280
300
320
340
x position (μm)
3
2&4
1
Distance from surface (nm)
0
0.1
0.5
1
10
50
c)
8.0E-6
6.0E-6
4.0E-6
2.0E-6
0.0
-2.0E-6
-4.0E-6
-6.0E-6
Acceleration (m/s²)
260
280
300
320
340
x position (μm)
3
2&4
1
Distance from suface (nm)
0
0.1
0.5
1
10
50

Figure S3.

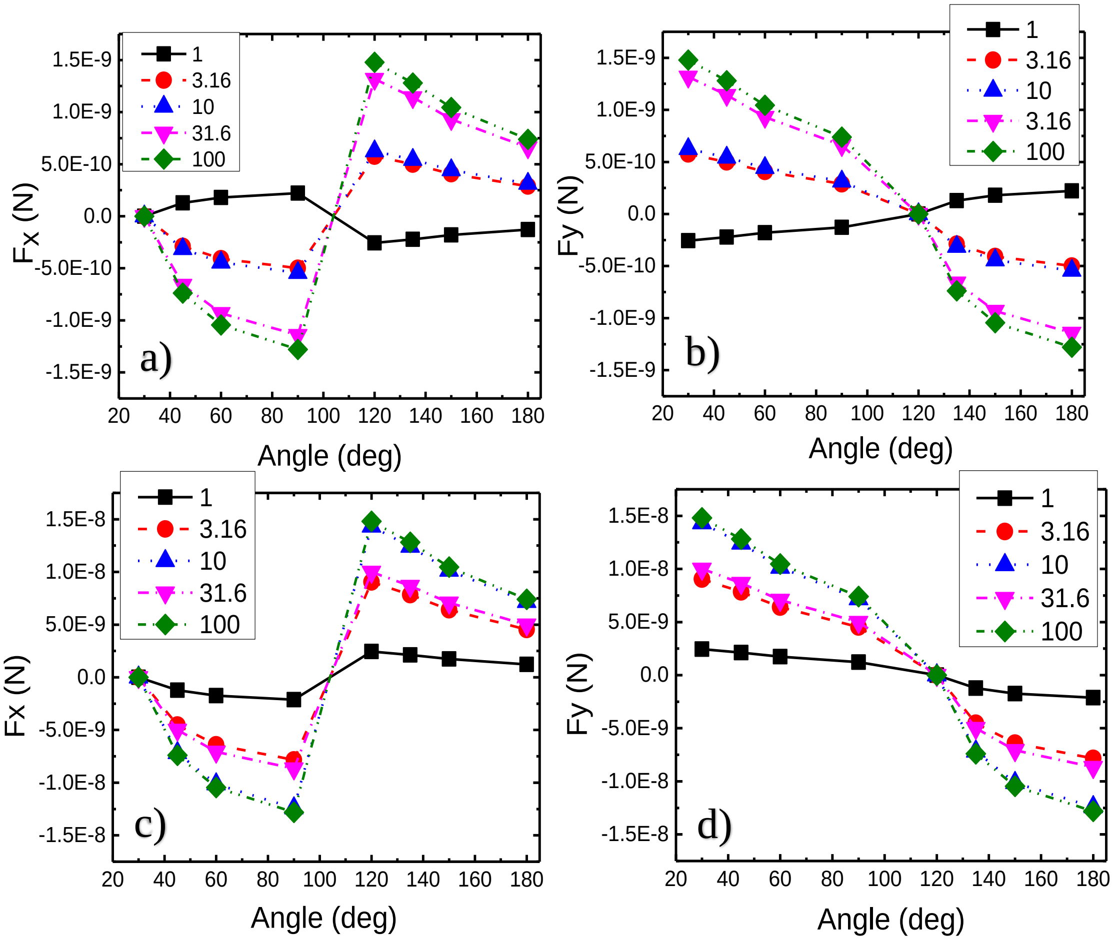
a)
Fx (N)
1.5E-9
1.0E-9
5.0E-10
0.0
-5.0E-10
-1.0E-9
-1.5E-9
Angle (deg)
20
40
60
80
100
120
140
160
180
1
3.16
10
31.6
100
b)
Fy (N)
1
3.16
10
3.16
100
c)
Fx (N)
1.5E-8
1.0E-8
5.0E-9
0.0
-5.0E-9
-1.0E-8
-1.5E-8
d)
Fy (N)

Notes and references:

1 Derjaguin, B.; Vlashenko, G. Dan sssr. *Coll. & Interf. Sci.* **1948**, *63*, 155.

2 Gregory, R.T.; Taylor, H.P. An oxygen isotope profile in a section of cretaceous oceanic-crust, samail ophiolite, oman - evidence for delta-18-o buffering of the oceans by deep (less-than 5 km) seawater-hydrothermal circulation at mid-ocean ridges. *J. Geophys. Res.* **1981**, *86*(B4), 2737-2755.

3 Hogg, R.; Healy, T.; Fuerstenau, D. Mutual coagulation of colloidal dispersions. *Trans. Faraday Soc.* **1966**, *62*, 1638-1651.

4 Israelachvili, J.N. *Intermolecular and Surface Forces: With Applications to Colloidal and Biological Systems (Colloid Science);* Academic press London, 1992.

5 Chinju, H.; Kuno, Y.; Nagasaki, S.; Tanaka, S. Deposition behavior of polystyrene latex particles on solid surfaces during migration through an artificial fracture in a granite rock sample. *J. Nucl. Sci. Technol.* **2001**, *38*(6), 439-443.

6 Prieve, D.C.; Ruckenstein, E. Effect of London forces upon the rate of deposition of Brownian particles. *AIChE Journal.* **1974**, *20*(6), 1178-1187.

7 Elimelech, M.; Jia, X.; Gregory, J.;Williams, R. *Particle deposition & aggregation: Measurement, modelling and simulation*. Butterworth-Heinemann, 1998.

8 Yao, K.-M.;Habibian, M.T.;O'Melia, C.R. Water and waste water filtration. Concepts and applications. *Environ. Sci. Technol.* **1971**, *5*, 1105-1112.

9 Levich, V.G. *Physicochemical hydrodynamics*. Prentice Hall, 1962.

10 Shames, I.H.;Shames, I.H. *Mechanics of fluids*. McGraw-Hill New York, 1982.

11 Lock, R., 1951. The velocity distribution in the laminar boundary layer between parallel streams. *The Quarterly Journal of Mechanics and Applied Mathematics*, *4*(1), pp.42-63.